This is an Accepted Manuscript of an article published by Taylor & Francis in Computer Methods in Biomechanics and Biomedical Engineering on 8 Feb 2018, available online: http://www.tandfonline.com/10.1080/10255842..2018.1437151.

The potential role of variations in juvenile hip geometry on the development of Legg-Calvé-Perthes disease: a biomechanical investigation

Manuel Pinheiro[1], Catherine A. Dobson[1], Nicholas M. Clarke[2] and Michael J. Fagan[1]

[1]Medical and Biological Research Group, School of Engineering, University of Hull, UK

[2]Paediatric Orthopaedics, University Hospitals Southampton NHS Foundation Trust, Southampton, UK

Abstract

Legg-Calvé-Perthes disease (LCP) is one of the most poorly understood diseases in paediatric orthopaedics. One common trait of LCP is the marked morphological difference between healthy and pathological hips, early deviations of which (i.e. prior to disease onset) have been suggested to lead to the overload and collapse of the epiphysis. Here, the impact of common variations in geometry is investigated with a finite element model of a juvenile femur under single leg standing and landing. Here, the impact of typical variations in geometry is investigated with a finite element model of a juvenile femur under single leg standing and landing. The variations appear to have only a limited effect on the stress distribution in the femoral epiphysis even during high impact activities. This suggests that, for this individual at least, they would be unlikely to cause epiphyseal overload and collapse, even in the presence of a skeletally immature epiphysis.

Keywords: Perthes disease; hip morphology; juvenile hip; biomechanics; finite element analysis

Introduction

Legg-Calvé-Perthes disease (LCP or Perthes') is commonly referred to as avascular necrosis of the femoral epiphysis, and is characterized by collapse and flattening of the femoral head. The disease was described more than 100 years ago by four studies carried out by Waldenström (1909), Legg (1910), Calvé (1910) and Perthes (1910). However, LCP remains one of the most poorly understood disorders in paediatric orthopaedics, and the underlying mechanisms that lead to the morphological changes in the pathological hip are yet unknown.

Several mechanisms have been suggested as potential precursors of Perthes', namely: single (Kim & Herring 2013) or multiple ischaemic events (Bruce & Perry 2014; Chaudhry et al. 2014); vascular deficiency or obstruction (Aksoy et al. 2008; Pinheiro et al. 2018); microvesiculation (Kocjančič el., 2014); coagulation disorders (Vosmaer et al. 2010); deviations in geometry (Pienkowski et al. 2009); growth impairment and skeletal immaturity (Kitoh et al. 2003; Chaudhry et al. 2014); socio-economic conditions and social deprivation (Perry et al. 2012); and genetic factors (Miyamoto et al. 2007).

Clinical observations showed that LCP develops in four stages, namely: osteonecrosis, fragmentation, re-ossification and healing, and the inability to recover the spherical shape during the re-ossification phase can lead to a permanent flattening of the femoral head, which may ultimately result in early osteoarthritis (Kim & Herring 2013). Early detection of the disease is fundamental in preventing this irreversible change in hip geometry, and to allow normal development thereafter. There is a general consensus about the ischaemic nature of LCP (Kim & Herring 2013), however the nature of the vascular insult is still unknown (Berthaume et al. 2016).

One of the most plausible triggers of the disease is the altered biomechanics differences observed between the healthy and pathological hip. The morphological variations include

lateral displacement of the femoral head, widening of the joint space, broadening and shortening of the femoral neck, widening and reduction of the acetabular depth, and flattening and subluxation of the femoral head. For instance, Pienkowski et al. (2009) observed a statistically significant difference between the femoral head size and acetabular radius in children (average age 8.2 years) with unilateral LCP, with the affected hips having greater femoral head size and acetabular radius, with the radius ratio between femoral head and acetabulum being smaller than in normal hips. The average centre-to-centre distance was also significantly higher in LCP (of 3.0 ± 1.3 (SD) mm) when compared with 1.2 ± 0.5 (SD) mm in the normal side. In addition, Huhnstock et al. (2014) analysed the changes in the acetabulum in children with unilateral LCP and observed that during the first year after the diagnosis. The acetabular depth-to-width ratio (ADR) decreased when compared with the normal hip, due to a decrease in depth of 10% and an increase in width of 10%. However, whether these differences are a cause or a consequence of the disease is still unclear. In addition, retardation of bone growth in the appendicular skeleton is also very common in LCP patients, typically of 1 to 2 years (Kim & Herring 2013).

Berthaume et al. (2016) proposed five hypotheses describing how Perthes' disease might develop through either epiphyseal vessel obstruction or femoral head overload arising from altered biomechanics. In this current paper, the possibility of the onset of LCP due to epiphyseal overload as a direct consequence of the morphological changes in the hip is investigated. To achieve this, typical morphological variations observed in the pathological hip are incorporated in the finite element model of a heathy 7.9-year-old male. Their impact is then investigated by comparing the mechanical loading observed in the normal and modified hips, in particular whether these changes are sufficient to cause the collapse of the femoral epiphysis.

Materials and Methods

A 3D FE model of a healthy male subject 7.9-years-old was created from computed tomography (CT) image data, with image segmentation carried out according to the protocol in (Pinheiro & Alves 2015). The hip is characterized by an acetabular radius of 21.5 mm femoral head radius 15.2 mm, angle of Wiberg of 23.5 degrees, and a centre-to-centre distance of approximately 0.5 mm, (which shows that it falls within the normal range of geometry for a child of that age (Than et al. 2004; Szuper et al. 2015). The pelvis and femurs were initially positioned in an upright position by computing the geometrical centres of the hip, knee and ankle along the same vertical line, both in the coronal and sagittal plane. The mechanical axis of the leg was then rotated to a single-leg stance position. Since the ankle data was not available, anthropometric relations between femur and tibia (Irving 2016) were used to estimate and positon the joint in the midline of the body (Fig. 1a).

Free-body Diagram Optimization

Two loading conditions were considered, namely standing on one-leg and single-leg landing (for example from jumping). For the single-leg stance position considered here, the knee reaction force (KJR) and ground reaction force (GRF) were both assumed to be equal to the body weight (BW), whereas for single-leg drop landing from a height of 30.0 cm the GRF is reported to be 2.94BW while the KJR can reach 8.13BW (Mokhtarzadeh et al. 2013). The muscle forces necessary to balance these external forces applied were computed using a non-linear static free-body diagram (FBD) optimization code developed in MATLAB R2014a (MathWorks, Massachusetts, USA). In the FBD protocol, all muscles were modelled as single lines of action connecting the centres of the origin and insertion areas of the muscles derived from the literature (Schünke et al. 2010). The physiological cross-section areas (PCSA) of each muscle were obtained from Handsfield et al. (2014) and Pierrynowski (1982), and scaled taking

into account a target body weight of 23.0 Kg (Lappin et al. 2003). To compute the maximum achievable force for each muscle (F_{max}^{i}) a specific tension of $133\ N/cm^2$ was considered (Lieber & Burkholder 2007), with FBD optimization applied to minimize muscle activation according to (Modenese et al. 2011):

$$minimize\ J(F_i) = \sum_{i=1}^{m} \left(\frac{F_i}{F_{max}^{i}} \right)^n \quad (1)$$

subject to:

$$\sum_{i=1}^{m} \vec{r}_{ij} \times \vec{F}_i = M_j \quad (2)$$

$$0 \leq F_i \leq F_{max}^{i}$$

where m is the number of muscles considered, F_{max}^{i} is the maximum force that muscle i can generate, $\vec{r}_{ij}$ is the moment arm of i^{th} muscle and M_j is the moment acting around the j^{th} axis (Modenese et al. 2011), and $n = 2$ to minimize the overall muscle activation (Kaufman et al. 1991). The 24 main muscles acting around the hip were represented individually, with the exception of the iliotibial band and the adductor minimus, which were combined with other muscle groups because of their parallel action with them (Fig. 1a).

Finite element model

The key anatomical structures of the normal, healthy juvenile hip considered in the FE models are shown in the cut-away view in Fig. 1b. Since the different cartilage layers weren't visible on the CT scan, the cartilage of the femoral head was defined by offsetting the epiphyseal surface by 2.0 mm, thereby matching the cartilage thickness reported in (Castriota-Scanderbeg & Micheli 1995) for a child of that age. The remainder of the cartilage volume was defined as

117 acetabular cartilage. The basic model was then modified to simulate some of the reported
118 morphological variations observed in LCP hips. In particular, hip joint incongruity was
119 considered through medial and lateral displacement of the femoral head by ± 3.0 mm
120 (Pienkowski et al. 2009), and a decrease in acetabular depth of 10% (1.7 mm) and an increase
121 in acetabular opening of 10% (2.0 mm) were examined (Huhnstock et al. 2014). Skeletal
122 immaturity was simulated by uniformly offsetting the boundary of the epiphysis by
123 approximately 2.30 mm throughout, which corresponds to skeletal immaturity of
124 approximately 2.0 years (Kitoh et al. 2003). The outlines of the different geometries are shown
125 schematically in Fig. 1c.

126 Muscle forces were applied to the centroid of the muscle insertion areas, whereas KJR was
127 applied to the geometrical centre of the knee. Symmetry was assumed along the sagittal plane,
128 and therefore only half the pelvis and one femur were modelled in the FE analyses. The models
129 were meshed with quadratic tetrahedral elements for solution in ANSYS v 15.0.7 (ANSYS,
130 Inc., Canonsburg, USA). The mesh was generated with a specified minimum edge length of
131 0.5 mm using the FE mesher vcat2tets (Labelle & Shewchuk 2007), and model convergence
132 was checked and confirmed with approximately 3.0 million elements (not reported here). All
133 materials were modelled as linear elastic, isotropic and homogeneous, with mechanical
134 properties summarized in Table 1. Fixed boundary conditions were applied to the surface of
135 the sacroiliac joint with symmetry boundary conditions applied to the pubic joint ensuring the
136 pelvis was not over-constrained. Additional constraints were added to the medial and lateral
137 condyles of the knee to avoid medio-lateral displacements arising from rounding errors and
138 inconsistencies in force mapping from the FBD to the FE model (Fig. 1a). To quantify the
139 amount of epiphyseal volume at risk of collapse the work of Hambli (2013) is considered,
140 where, for the trabecular bone elastic modulus of 1500 MPa considered in this work (Table 1,

141 $BV/TV = 28.2\%$ (Yang et al. 1999), the ultimate compressive stress is estimated to be
142 approximately 20.8 MPa (Hambli 2013).

143

144 **Results**

145 ***Muscle activation and hip reaction force***

146 Table 2 compares the forces predicted in the 8 muscles with the largest muscle activation values
147 for the different model variations. The main muscle activations were observed in the gluteus
148 medius and minumus, tensor fascia, rectus femoris and psoas. Moving the femoral head from
149 a medial position to a more lateral position increases all muscle activities with the exception of
150 the rectus femoris which decreases slightly. The changes in muscle activation due to the change
151 in the geometry of the acetabular roof are minimal compared to the reference model (hence are
152 not included). In single-leg landing, there is a significant increase in muscle recruitment,
153 especially in the gluteus medius, tensor fascia and psoas muscle (Table 2). The hip joint
154 reaction (HJR) force is generally insensitive to model variation, and changes only slightly with
155 femoral head position (Table 3). For example, there is a 3.57% decrease for 3.0mm medial
156 displacement of the femoral head and a 2.68% increase for an equivalent lateral displacement.
157 Conversely, jumping and landing on one-leg increases the HJR force by a factor of 5.6, when
158 compared with the reference single-leg stance model.

159 ***Epiphyseal stress***

160 Fig. 2 shows the distribution of von Mises stress through the femoral head for all the
161 morphological changes considered. In the reference model (Fig. 2a), the peak von Mises stress
162 is found to be 4.0MPa at the lower edge of the epiphysis. Medial displacement of the femoral
163 head decreases the stress in the trabecular bone (Fig. 2b), whereas lateral displacement

increases it throughout the femoral epiphysis (Fig. 2c). Little change is observed when the depth and width of the acetabulum were changed (Fig. 2d-e). For the skeletally immature epiphysis, a maximum von Mises stress of approximately 9.0 MPa was observed at the lower edge of the epiphysis (Fig. 2f).

In Fig. 3 the von Mises stress through the femoral epiphysis during landing are shown. Again, skeletal immaturity and the lateral displacement lead to an increase of the stress in the ossified epiphysis, when compared to the reference (Fig. 3b-c). For the skeletally immature epiphysis the percentage of volume above the failure limit of 20.8 MPa is approximately 10.0% of the ossified volume, whereas for the laterally displaced version, only 2.0% of the ossified volume is above the critical value.

The relative effects of the geometry variants are summarized in the difference plots between the reference (normal) and customised models (Fig. 4a-e). Positive values indicate higher stresses in the reference model (i.e. a model variation model leads to lower stresses), whereas negative values correspond to higher stresses in a model variation. Only subtle differences were observed between the normal hip and the pathological hips. The highest differences are clearly observed in the superior aspect of the epiphyseal cartilage. The stress values in the lateral surface of the epiphysis remained mostly unchanged in all cases (Fig. 4). Only slight variations (smaller than ±1.0 MPa) in the equivalent stress were observed in the femoral head for standing in one-leg (Fig. 4a-b, comparison between Fig. 2a-2b and Fig.2a-2c), whereas in single-leg landing they reached approximately ±5.0 MPa (Fig. 4c-d, comparison between Fig. 3a-2c and Fig.3a-2d).

Discussion

A 3D FE model was developed to investigate the biomechanical implications of the main morphological changes observed in LCP disease. The biomechanical changes across the femoral epiphysis were assessed by comparing the stresses predicted in the healthy juvenile hip model with the morphologically altered models (Fig. 1c). A 3D musculoskeletal model of a 7.9-years-old male was developed, considering 24 muscles of the thigh. FBD optimization was employed to determine the muscle activations and HJR forces for standing and drop landing in one-leg.

There are several simplifications in the model which need further comment. Firstly, all materials were modelled as homogeneous and linear elastic, but both bone and cartilage are known to exhibit non-isotropic behaviour (Cohen et al. 1998). For the bone, subtle site-specific variations in material properties based on CT grey scale values could have been included in the reference model, but then an assumption would have had to be made regarding the distribution of property values in the skeletally immature version. Rather than detecting those differences and generally confounding the effects of the geometry variations, it was therefore decided that it would be better to use uniform property values derived from juvenile subjects (Ohman et al. 2011). Similarly, individual-specific cartilage properties were unknown, and again to avoid the confounding effect of using arbitrary values, the use of a constant value was again considered to be most appropriate in this study, especially when differences rather than absolute values are of primary interest.

Information regarding HJR forces acting in the juvenile hip is extremely scarce. Heimkes et al. (1993) developed a 2D model of the hip and simulated a single-leg stance, whereas Carriero et al. (2012) performed 3D gait study of healthy children with ages between 6 – 12 years old. Similar HJR forces were obtained in both studies (3.10BW and 3.05BW, respectively), while

in the current study a HJR of 3.34 ± 0.02BW was predicted for a one-legged stance. These values compare well with the juvenile values, but interestingly are all higher than the data recorded for adults for both walking and standing on one leg (of typically 2.38BW (Bergmann et al. 1993)).

In single-leg landing the HJR force in this juvenile model was predicted to be 19.07 ± 0.70BW. Under extreme conditions joint reaction forces in adults may also reach high values. For example, peak GRF and KJR forces up to 10BW have been measured during jumping exercises (McNair & Prapavessis 1999) and plyometric training (Jensen 2005), whereas HJR forces of 10BW were recorded during stumbling (Bergmann et al. 2004) and values up to 15BW during vigorous exercise are documented in the literature (Loudon et al. 2013). The differences are again interesting, but there is no reason to expect similar HJR values in juveniles and adults when differences in the relative dimensions of juvenile and adult hips and BWs are considered.

For the individual considered in this current study, the results show that the morphological changes considered in this analysis have a limited impact on the stress distribution in the femoral epiphysis (Fig. 2). Although individual components are affected differently (the horizontal component increases by approximately 30% through just 3.0mm of lateral displacement (Table 3)), the overall HJR increases by less than 3%. The loading of the femoral head is therefore clearly modified, but he overall effect appears to be insufficient to cause failure directly. With the rather extreme case of single-leg landing, the stress levels do show an increase due to the significant increase in load, and when combined with a skeletally immature epiphysis, approximately 10% of the epiphysis may experience a stress above the estimated ultimate stress (Fig. 3). However, Nishii et al. (2002) and Lieberman et al. (2012) observed that tissue necrosis should account for approximately 30% of the adult femoral head volume to

cause epiphyseal collapse. Although not directly comparable, this value provides an indication of the extent of epiphyseal compromise necessary for the failure of the femoral head.

The results suggest that morphological changes have a limited impact in the stress across the epiphysis (Fig. 4), and that even a skeletally immature epiphysis does not seem to be overload even in drop-landing. Similarly, because such a small proportion of the epiphysis is overloaded, the results do not provide significant evidence to support the alternative sequence of events that lead to Perthes' proposed by Berthaume et al. (2016), (hypothesis H3), where the overload of the immature epiphysis leads to failure, vascular occlusion and the development of LCP. Additional investigations need to be conducted to further confirm these results, especially with younger patients, since the initial trigger for the disease may occur at a younger age. A more advanced FE model incorporating the main epiphyseal arteries may also be an invaluable tool to evaluate the likelihood of vessel damage or obstruction as they travel up to and through the articular cartilage.

Acknowledgement

This project was supported by generous grants from The Henry Smith Charity and Action Medical Research (research grant: GN2076).

Conflict of Interest Statement

There is no conflict of interests to declare.

References

Aksoy MC, Aksoy DY, Haznedaroglu IC, Sayınalp N, Kirazli S, Alpaslan M. 2008. Thrombomodulin and GFC levels in Legg–Calve–Perthes disease. Hematology. 13:324–328.

Bergmann G, Graichen F, Rohlmann A. 1993. Hip joint loading during walking and running, measured in two patients. J Biomech. 26:969–990.

Bergmann G, Graichen F, Rohlmann A. 2004. Hip joint contact forces during stumbling. Langenbeck's Arch Surg. 389:53–59.

Berthaume MA, Perry DC, Dobson CA, Witzel U, Clarke NM, Fagan MJ. 2016. Skeletal immaturity, rostral sparing, and disparate hip morphologies as biomechanical causes for Legg-Calvé-Perthes' disease. Clin Anat. 29:759–772.

Bruce C, Perry DC. 2014. Legg-Calvé-Perthes' disease. In: Bentley G, editor. Eur Surg Orthop Traumatol EFORT Textb. Berlin, Heidelberg: Springer Berlin Heidelberg; p. 4443–4468.

Calvé J. 1910. Sur une forme particulière de pseudo-coxalgie greffée sur des déformations caractéristiques de l'extrémité supérieure du fémur. Rev Chir. 42:54–84.

Carriero A, Zavatsky A, Stebbins J, Theologis T, Lenaerts G, Jonkers I, Shefelbine SJ. 2012. Influence of altered gait patterns on the hip joint contact forces. Comput Methods Biomech Biomed Engin. 17:1–8.

Castriota-Scanderbeg A, Micheli V De. 1995. Ultrasound of femoral head cartilage: a new method of assessing bone age. Skeletal Radiol. 24:197–200.

Chaudhry S, Phillips D, Feldman D. 2014. Legg-Calvé-Perthes Disease An Overview with Recent Literature. Bull Hosp Joint Dis. 72:18–27.

Cohen B, Lai WM, Mow VC. 1998. A transversely isotropic biphasic model for unconfined compression of growth plate and chondroepiphysis. J Biomech Eng. 120:491–496.

Hambli R. 2013. Micro-CT finite element model and experimental validation of trabecular bone damage and fracture. Bone. 56:363–374.

Handsfield GG, Meyer CH, Hart JM, Abel MF, Blemker SS. 2014. Relationships of 35 lower limb muscles to height and body mass quantified using MRI. J Biomech. 47:631–638.

Heimkes B, Posel P, Plitz W, Jansson V. 1993. Forces acting on the juvenile hip joint in the one-legged stance. J Pediatr Orthop. 13:431–436.

283 Huhnstock S, Svenningsen S, Pripp AH, Terjesen T, Wiig O. 2014. The acetabulum in Perthes'
284 disease: a prospective study of 123 children. J Child Orthop. 8:457–465.

285 Irving PH. 2016. Terminology, the Standard Human, and Scaling. In: Phys Hum Body. 3rd ed.
286 New York, USA: Springer International Publishing; p. 1–26.

287 Jensen RL. 2005. Ground and knee joint reaction forces during variations of plyometric
288 exercises. In: Wang Q, editor. XXIII Int Symp Biomech Sport. Beijing: International Society
289 of Biomechanics; p. 373–376.

290 Kaufman KR, Au KN, Litchy WJ, Chao EYS. 1991. Physiological prediction of muscle forces-
291 II. Application to isokinetic exercise. Neuroscience. 40:793–804.

292 Kim HKW, Herring JA. 2013. Legg-Calvé-Perthes' disease. In: Herring JA, editor. Tachdjian's
293 Pediatr Orthop from Texas Scottish Rite Hosp Child. 5th ed. Texas: Elsevier; p. 580–629.

294 Kitoh H, Kitakoji T, Katoh M, Takamine Y. 2003. Delayed ossification of the proximal capital
295 femoral epiphysis in Legg-Calvé-Perthes' disease. J Bone Joint Surg Br. 85:121–124.

296 Labelle F, Shewchuk J. 2007. Isosurface stuffing: fast tetrahedral meshes with good dihedral
297 angles. ACM Trans Graph. 26:1–10.

298 Lappin K, Kealey D, Cosgrove A, Graham K. 2003. Does low birthweight predispose to
299 Perthes' disease? Perthes' disease in twins. J Pediatr Orthop B. 12:307–10.

300 Legg AT. 1910. An Obscure Affection of the Hip-Joint. Bost Med Surg J. 162:202–204.

301 Lieber RL, Burkholder TJ. 2007. Musculoskeletal soft tissue mechanics. In: Peterson DR,
302 Bronzino JD, editors. Biomech Princ Appl. 2nd ed. New York, USA: CRC Press; p. 1–13.

303 Lieberman JR, Engstrom SM, Meneghini RM, Soohoo NF. 2012. Which factors influence
304 preservation of the osteonecrotic femoral head? Clin Orthop Relat Res. 470:525–534.

305 Loudon JK, Manske RC, Reiman MP. 2013. Hip. In: Clin Mech Kinesiol. Champaign, IL USA:
306 Human Kinetics; p. 439.

307 McNair PJ, Prapavessis H. 1999. Normative data of vertical ground reaction forces during
308 landing from a jump. J Sci Med Sport. 2:86–88.

309 Miyamoto Y, Matsuda T, Kitoh H, Haga N, Ohashi H, Nishimura G, Ikegawa S. 2007. A
310 recurrent mutation in type II collagen gene causes Legg-Calve-Perthes disease in a Japanese
311 family. Hum Genet. 121:625–629.

312 Modenese L, Phillips ATM, Bull AMJ. 2011. An open source lower limb model: Hip joint
313 validation. J Biomech. 44:2185–2193.

314 Mokhtarzadeh H, Yeow CH, Hong Goh JC, Oetomo D, Malekipour F, Lee PVS. 2013.
315 Contributions of the Soleus and Gastrocnemius muscles to the anterior cruciate ligament
316 loading during single-leg landing. J Biomech. 46:1913–1920.

317 Nishii T, Sugano N, Ohzono K, Sakai T, Sato Y, Yoshikawa H. 2002. Significance of lesion
318 size and location in the prediction of collapse of osteonecrosis of the femoral head: a new three-
319 dimensional quantification using magnetic resonance imaging. J Orthop Res. 20:130–6.

320 Ohman C, Baleani M, Pani C, Taddei F, Alberghini M, Viceconti M, Manfrini M. 2011.
321 Compressive behaviour of child and adult cortical bone. Bone. 49:769–776.

322 Perry DC, Machin DMG, Pope D, Bruce CE, Dangerfield P, Platt MJ, Hall AJ. 2012. Racial
323 and geographic factors in the incidence of Legg-Calvé-Perthes' disease: a systematic review.
324 Am J Epidemiol. 175:159–66.

325 Perthes G. 1910. Über Arthritis deformans juvenilis. Deutsch Zeitschr Chir. 107:111–159.

326 Pienkowski D, Resig J, Talwalkar V, Tylkowski C. 2009. Novel three-dimensional MRI
327 technique for study of cartilaginous hip surfaces in Legg-Calvé-Perthes disease. J Orthop Res.
328 27:981–8.

329 Pierrynowski MR. 1982. A physiological model for the solution of individual muscle forces
330 during normal human walking. [place unknown]: Simon Fraser University, Canadá.

331 Pinheiro M, Alves JL. 2015. A new level-set based protocol for accurate bone segmentation
332 from CT imaging. IEEE Access. 3:1894–1906.

333 Pinheiro M, Dobson CA, Perry DC, Fagan MJ. 2018. New insights into the biomechanics of
334 Legg-Calvé-Perthes' disease: The role of epiphyseal skeletal immaturity in vascular
335 obstruction. Bone Joint Res. 7.

336 Schünke M, Ross LM, Schulte E, Schumacher U, Lamperti ED. 2010. The Lower Limb. In:
337 Lawrence M. Ross EDL, editor. Thieme Atlas Anat Gen Anat Musculoskelet Syst. 2nd ed.
338 Texas: Thieme; p. 360–483.

339 Szuper K, Schlégl ÁT, Leidecker E, Vermes C, Somoskeöy S, Than P. 2015. Three-
340 dimensional quantitative analysis of the proximal femur and the pelvis in children and
341 adolescents using an upright biplanar slot-scanning X-ray system. Pediatr Radiol. 45:411–421.

342 Than P, Sillinger T, Kránicz J, Bellyei Á. 2004. Radiographic parameters of the hip joint from
343 birth to adolescence. Pediatr Radiol. 34:237–244.

344 Vosmaer A, Pereira RR, Koenderman JS, Rosendaal FR, Cannegieter SC. 2010. Coagulation
345 Abnormalities in Legg-Calvé-Perthes Disease. J Bone Jt Surg. 92:121–128.

346 Waldenström H. 1909. Der obere tuberkulose collumherd. Zeitschrf Orthop Chir. 24:487–512.

347 Yang G, Kabel J, Van Rietbergen B, Odgaard A, Huiskes R, Cowin SC. 1999. Anisotropic
348 Hooke's law for cancellous bone and wood. J Elast. 53:125–146.

349 Zhao Y, Li J, Wang D, Liu Y, Tan J, Zhang S. 2012. Comparison of stability of two kinds of
350 sacro-iliac screws in the fixation of bilateral sacral fractures in a finite element model. Injury.
351 43:490–494.

352

353

354 Table 1: Material properties (Yang et al. 1999; Ohman et al. 2011; Zhao et al. 2012; Hambli
355 2013).

Material properties	Cortical bone	Trabecular bone	Epiphyseal/acetabular cartilage	Pubic symphysis	Triradiate cartilage
Young's modulus (MPa)	11880	1500	1.50	5.00	5.00
Poisson's ratio	0.300	0.300	0.495	0.450	0.495

356

357

358

Table 2: Muscle activation forces for the 8 primary muscles for the reference, medial displacement and lateral displacement models when standing on one leg, together with the forces in the reference model in single leg landing (with percent muscle activations displayed in brackets).

	Muscle activation in N (% activation)			
Muscle	**Reference**	**-3.0 mm medial**	**+3.0 mm lateral**	**Single-leg landing**
Gluteus medius	325.8 (17%)	299.0 (15%)	346.9 (18%)	1328.4 (68%)
Gluteus minimus	28.1 (8%)	22.6 (6%)	32.7 (9%)	3.5 (1%)
Tensor fascia latae	45.5 (27%)	36.5 (21%)	53.1 (31%)	334.1 (98%)
Rectus femoris	102.3 (7%)	103.4 (7%)	93.3 (6%)	394.1 (26%)
Vastus Intermedius	27.0 (2%)	14.4 (1%)	28.6 (2%)	16.4 (1%)
Psoas	56.2 (8%)	52.9 (7%)	56.7 (8%)	584.5 (83%)
Iliacus	31.2 (6%)	30.1 (6%)	31.8 (6%)	5.1 (1%)
Semi-membranous	21.3 (1%)	28.2 (2%)	17.9 (1%)	15.9 (1%)

366 Table 3: Resultant hip joint reaction (HJR) force and its orthogonal components for the
367 different morphological changes applied to the normal hip geometry.

Morphological change	**H_x (×BW)**	**H_y (×BW)**	**H_z (×BW)**	**HJR (×BW)**	**Diff. (%)**
Reference model	0.44	0.33	3.31	3.36	-
Medial displacement: -3.0 mm	0.31	0.28	3.22	3.24	-3.57
Lateral displacement: +3.0 mm	0.57	0.34	3.39	3.45	+2.68
Acetabular Depth: -10%	0.42	0.30	3.29	3.33	-0.89
Acetabular Width: +10%	0.42	0.30	3.30	3.34	-0.59
Single-leg landing	2.03	2.05	18.85	19.07	+568.41

368

369

370

371

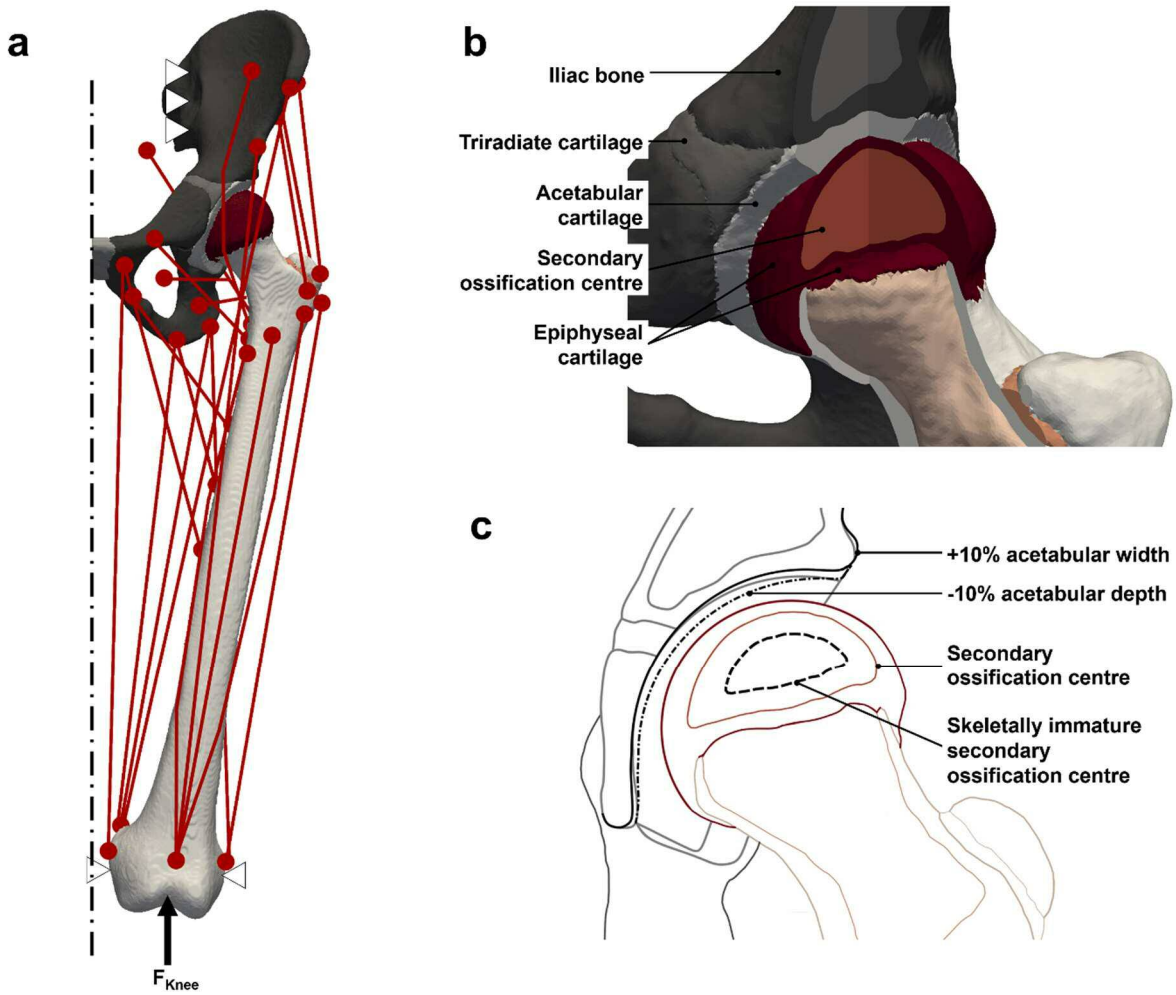

372

373 Fig. 1: (a) Schematic of the musculoskeletal model of the juvenile hip, consisting of the left
374 hemi-pelvis and femur and 24 muscles of the thigh; (b) section through the acetabulum and
375 femoral head showing the key structures of the joint; and (c) schematic of the key variations in
376 geometries of the different models.

377

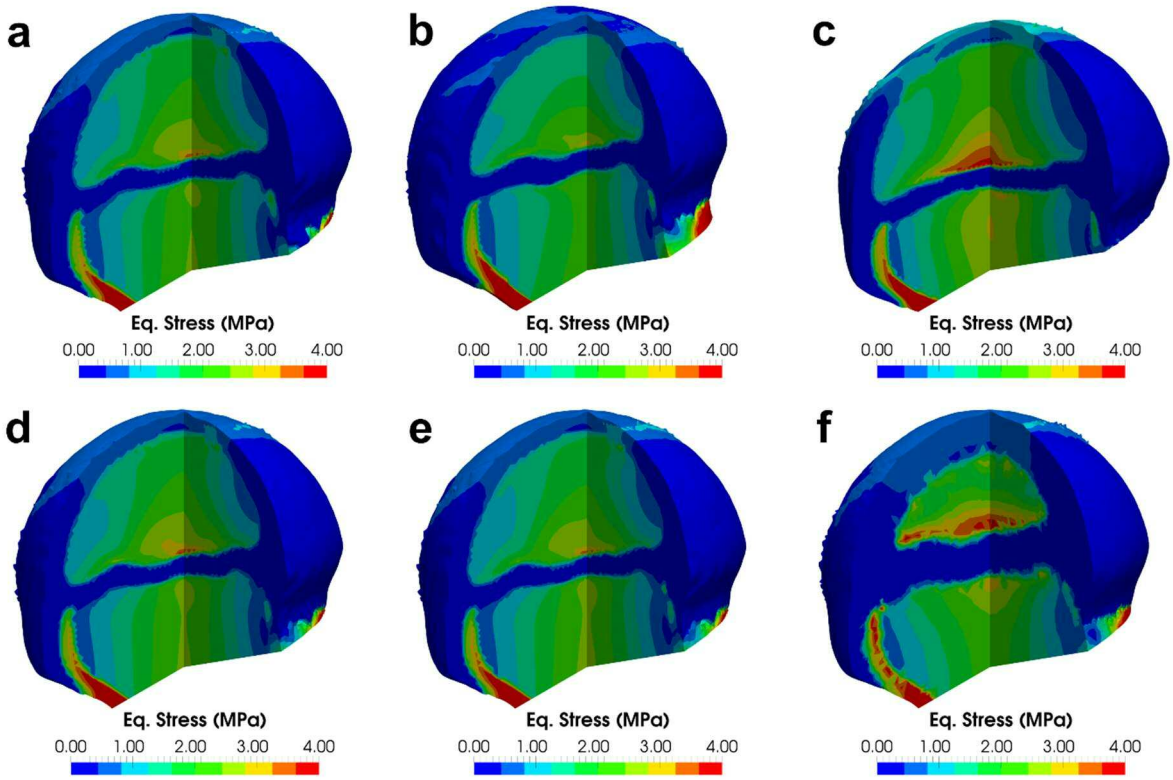

Fig. 2: Equivalent von Mises stresses (MPa) in the femoral epiphysis for standing on one-leg for the (a) reference model, (b) 3.0 mm medial displacement, (c) 3.0 mm lateral displacement, (d) 10% shallower acetabulum, (e) -10% wider acetabular opening, and (f) skeletally immature epiphysis.

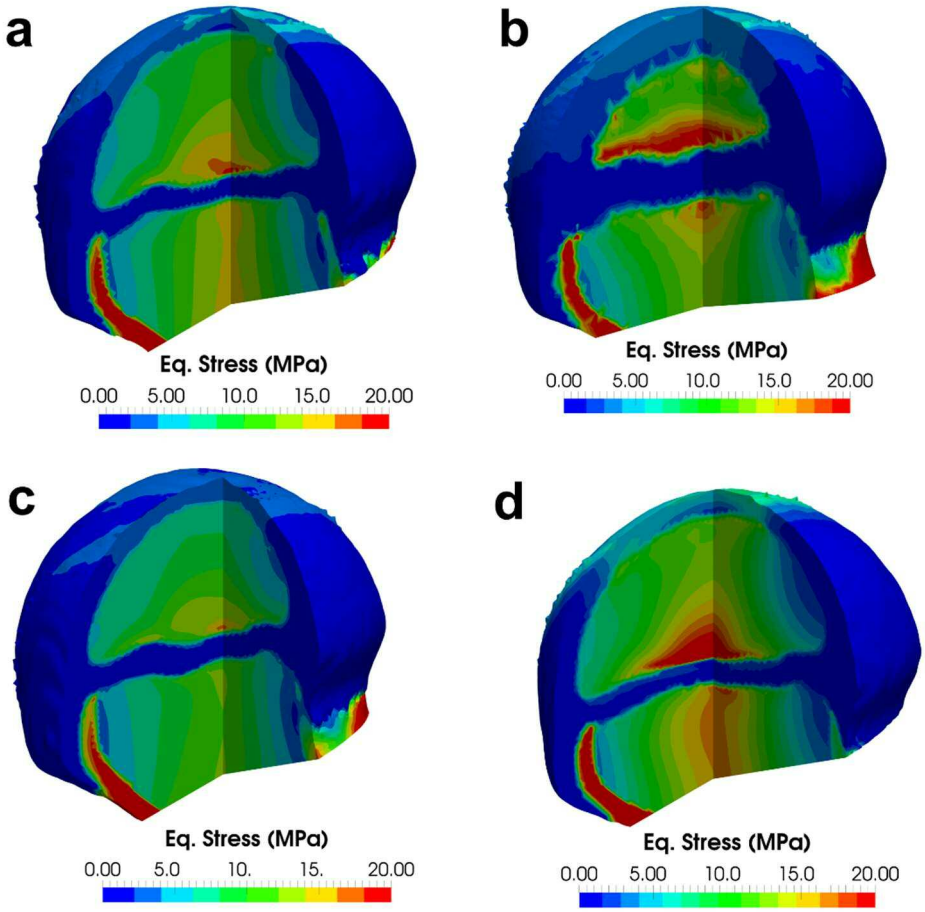

384

385 Fig. 3: Equivalent von Mises stresses (MPa) along the femoral epiphysis for landing on one-
386 leg for (a) the reference model and (b) the skeletally immature model, (c) 3.0 mm of medial
387 displacement and (d) 3.0 mm of lateral femoral head displacement.

388

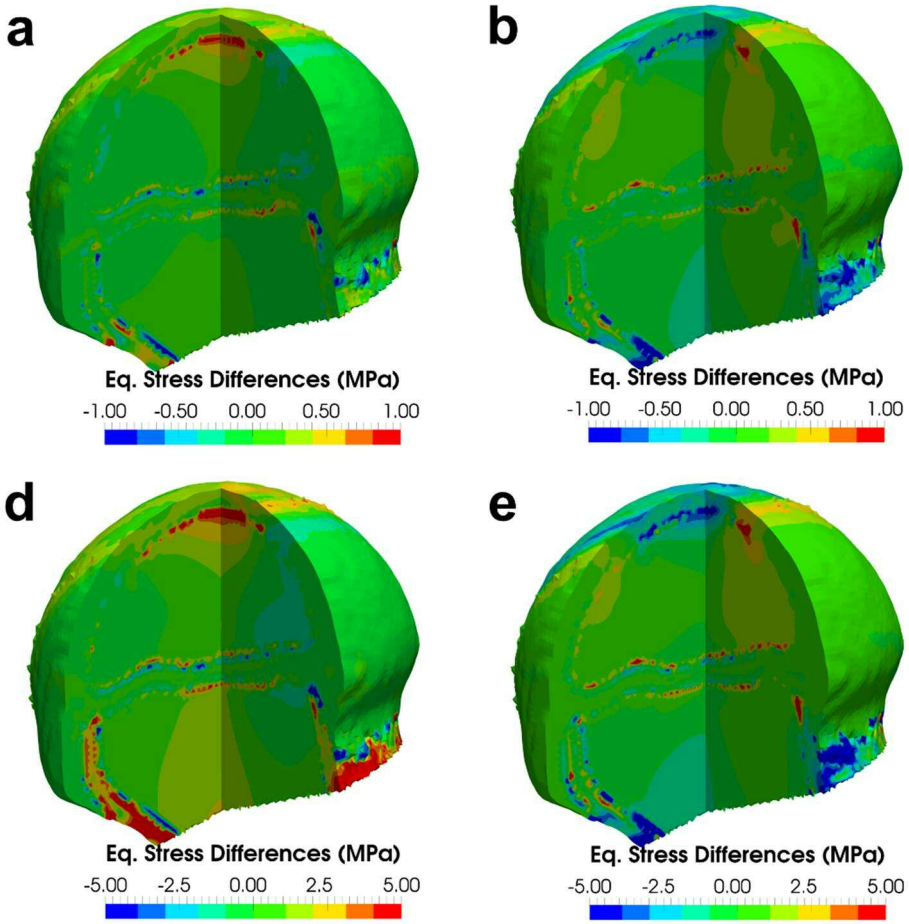

389

390 Fig. 4: Difference plots for the equivalent von Mises stresses (MPa) for standing on one leg
391 between the reference and (a) the 3.0 mm medial displacement model, (b) the 3.0 mm lateral
392 displacement, and for landing on one leg between the reference and (c) the 3.0 mm medial
393 displacement, (d) the 3.0 mm lateral displacement (positive differences correspond to higher
394 stresses in the reference model, while negative differences correspond to higher stresses in the
395 altered model).

396